

Impacts of Nuclear Burning on Reviving Weak Shocks of Neutrino-Driven Supernova Explosions

Ko Nakamura¹, Tomoya Takiwaki², Kei Kotake^{1,2}, and Nobuya Nishimura^{3,4}

ABSTRACT

We explore potential impacts of nuclear burning on assisting an onset of the neutrino-driven explosions of core-collapse supernovae. By changing the neutrino luminosity and its decay time to obtain parametric explosions in one-(1D) and two-dimensional (2D) models with or without a 13-isotope α network, we study how the inclusion of nuclear burning could affect the postbounce dynamics for four progenitor models; three for 15.0 M_{\odot} stars of Limongi & Chieffi (2006), Woosley & Weaver (1995), and Woosley et al. (2002) and one for an 11.2 M_{\odot} star of Woosley et al. (2002). We find that the energy supply due to nuclear burning of infalling material behind the shock can energize the shock expansion especially for models that produce only marginal explosions in the absence of nuclear burning. These models enjoy the assistance from nuclear burning typically in the following two ways, whether the shock front passes through the silicon-rich layer, or later it touches to the oxygen-rich layer. Depending on the neutrino luminosity and its decay time, the explosion energy increases up to a few times 10^{50} erg for models with nuclear burning compared to the corresponding models without. The difference in the explosion energy is generally smaller in 2D than in 1D, because neutrino-driven convection and the SASI in 2D models enhance the neutrino heating efficiency, which makes the contribution of nuclear burning relatively smaller compared to 1D models. We point out that these features are remarkable only for the Limongi-Chieffi progenitor both in 1D and 2D, which possesses a massive oxygen layer with its inner-edge radius being smallest among the employed progenitors, so that the shock can touch to the rich fuel on a shorter timescale after bounce. Considering uncertainties in progenitor models,

¹Division of Theoretical Astronomy, National Astronomical Observatory of Japan, 2-21-1 Osawa, Mitaka, Tokyo, 181-8588, Japan

²Center for Computational Astrophysics, National Astronomical Observatory of Japan, 2-21-1 Osawa, Mitaka, Tokyo, 181-8588, Japan

³Department Physik, Universität Basel, Klingelbergstrasse 82, 4056 Basel, Switzerland

⁴GSI, Helmholtzzentrum für Schwerionenforschung GmbH, Planckstraße 1, 64291 Darmstadt, Germany

our results indicate that nuclear burning should remain as one of the unignorable ingredients to foster the onset of neutrino-driven explosions.

Subject headings: supernovae: general — neutrinos — hydrodynamics — nuclear reactions, nucleosynthesis, abundances

1. Introduction

Ever since the dawn of modern core-collapse supernova (CCSN) theory, the neutrino-heating mechanism (Colgate & White 1966), in which a supernova shock is revived by neutrino energy deposition to trigger explosions (Wilson 1985; Bethe & Wilson 1985), has been the leading candidate for the explosion mechanism for more than four decades. However, the simplest, spherically-symmetric (1D) form of this mechanism fails, except for super-AGB stars at the low-mass end (Kitaura et al. 2006), to explode canonical massive stars (Rampp & Janka 2000; Liebendörfer et al. 2001; Thompson et al. 2003; Sumiyoshi et al. 2005). Pushed by accumulating supernova observations of the blast morphology (e.g., Wang & Wheeler 2008; Tanaka et al. 2012, and references therein), a number of multi-dimensional (multi-D) hydrodynamic simulations have been reported so far, which gives us a confidence that hydrodynamic motions associated with convection (e.g., Herant et al. 1992; Burrows et al. 1995; Janka & Müller 1996; Fryer et al. 2002; Fryer 2004) and the Standing-Accretion-Shock-Instability (SASI, e.g., Blondin et al. 2003; Scheck et al. 2004, 2006; Ohnishi et al. 2006, 2007; Foglizzo et al. 2006, 2007, 2012; Iwakami et al. 2008, 2009; Fernández & Thompson 2009a,b; Fernández 2010; Hanke et al. 2011; Müller et al. 2012b) can help the onset of the neutrino-driven explosion (see collective references in Janka 2012; Kotake et al. 2012).

In fact, the neutrino-driven explosions have been obtained in the following first-principle two-(2D) and three-(3D) dimensional simulations in which the spectral neutrino transport is solved by various approximations (e.g., Kotake et al. (2012)). Among them are the work by the Garching group (Buras et al. 2006a,b; Marek & Janka 2009; Müller et al. 2011, 2012a) who included one of the best available neutrino transfer approximations by the ray-by-ray variable Eddington factor method, by the Oak Ridge group (Bruenn et al. 2010) who included a ray-by-ray multi-group flux-limited diffusion transport with the best available weak interactions, and by our group (Suwa et al. 2010, 2011; Takiwaki et al. 2012) who employed a ray-by-ray isotropic diffusion source approximation (Liebendörfer et al. 2009)

with a reduced set of weak interactions¹.

This success, however, is accompanying further new questions. First of all, the explosion energies obtained in these 2D simulations are typically underpowered by one or two orders of magnitudes to explain the canonical supernova kinetic energy ($\sim 10^{51}$ erg, see table 1 in Kotake (2011) for a summary). Moreover, the softest version of Lattimer & Swesty (LS) equation of state (EOS) (Lattimer & Swesty 1991) with an incompressibility at nuclear density, K , of 180 MeV, have been often employed (see, however, Müller et al. (2012a)). A serious flaw is that the LS180 EOS cannot support a $2M_{\odot}$ cold neutron star which certainly exists in the universe (Demorest et al. 2010; Steiner et al. 2010)².

What on earth is missing furthermore? 3D hydrodynamics has been pointed out to foster the onset of neutrino-driven explosions compared to 2D (Nordhaus et al. 2010), although it is still under considerable debate (Hanke et al. 2011; Takiwaki et al. 2012). Very recently, general relativity has been reported to help the onset of multi-D neutrino-driven explosions by Müller et al. (2012a,b, 2011) in 2D simulations with detailed neutrino transport and by Kuroda et al. (2012) in 3D simulations but with approximate neutrino transport. Impacts of nuclear EOSs in the multi-D context have been investigated by Marek & Janka (2009); Marek et al. (2009) and Suwa et al. (2012)³. However, there may still remain further room to study more detailed nuclear physical impacts in these first principle multi-D simulations, such as the density dependence of symmetry energy and the skewness of compressibility (Steiner et al. 2010; Lattimer & Lim 2012) and influences of light nuclei (e.g., Sumiyoshi & Röpke 2008; Arcones et al. 2008; Nakamura et al. 2009) and of inelastic neutrino-nucleus scattering (e.g., Haxton 1988; Ohnishi et al. 2007; Langanke et al. 2008) on enhancing the neutrino heating rates in the gain region. The neutrino-driven mechanism would be assisted by other candidate mechanisms such as the acoustic mechanism (e.g., Burrows et al. 2006) or the magnetohydrodynamic mechanism (e.g., Kotake et al. (2004a,b); Takiwaki et al. (2004, 2009); Burrows et al. (2007a); Guilet et al. (2011); Obergaulinger & Janka (2011); Takiwaki & Kotake (2011), see also Kotake et al. (2006) for collective references therein). Other possibilities include QCD phase transitions in the core of the protoneutron star (e.g., Takahara & Sato 1988; Sagert et al. 2009) viscous heating by the magnetorotational instability (Thompson et al. 2005), or energy dissipation via Alfvén waves (Suzuki et al. 2008).

¹See Sumiyoshi & Yamada (2012) for collective references about detailed neutrino transport schemes.

²The maximum mass for the LS180 EOS is about $1.8M_{\odot}$ (e.g., O’Connor & Ott (2011); Kiuchi & Kotake (2008)).

³see also Couch (2012) in which the EOS impact has been studied in parametrized 2D models.

Joining in these efforts to look for some possible missing ingredients, we explore in this study potential impacts of nuclear burning on fostering the onset of the neutrino-driven explosions. To the best of our knowledge, Janka et al. (2001) were the first to clearly point out that an additional energy released by nuclear burning of infalling material behind the shock could make a significant contribution to affect the explosion energy (see their Eq.(5)). The mass in the silicon (Si) layer, depending sensitively on the progenitor masses and structures, is in the range of $\sim 0.3 - 0.6 M_{\odot}$ (Woosley & Weaver 1995; Woosley et al. 2002; Limongi & Chieffi 2006). Since the release of nuclear energy per gram in Si burning is $\approx 10^{18}$ erg/g, the nuclear energy E_{nuc} of a few 10^{50} erg is expected to be deposited by the explosive nuclear burning. However, Janka et al. (2001) hypothesized that based on an order-of-magnitude estimation, the energy gain by the nuclear burning might not significantly affect the explosion dynamics for progenitors above $20 M_{\odot}$, because the gravitational binding energy of the overlying, outward accelerated stellar layers outside the iron core, could be roughly the same order of E_{nuc} , possibly leading to the cancellation of the two effects. The Oak Ridge group (Bruenn et al. 2006; Mezzacappa et al. 2007) obtained explosions in their 2D radiation-hydrodynamic simulations for $11.2 M_{\odot}$ and $15.0 M_{\odot}$ stars, only when an alpha network calculation was included. They pointed out that the oxygen burning assists the (weak) shock to move farther out due to the additional pressure support in the vicinity of the shock.

In the present work, we take the following strategy to investigate the possible influence of nuclear burning on the neutrino-heating mechanism. Firstly we try, in the spirit of Burrows & Goshy (1993) and Janka (2001), to find a critical condition in 1D, in which nuclear burning affects the criteria of explosion. For the sake of our systematic survey, we employ a light-bulb scheme to trigger explosions (e.g., Janka & Müller 1996). Previously the role of nuclear burning seems to be considered as negligible using a very limited set of progenitor models (for example, see discussions in Nordhaus et al. 2010), but we will show that for a virgin progenitor model, nuclear burning can really push the weak shock farther out to help explosions. After we first give a detailed explanation in 1D models how nuclear burning could affect the postbounce dynamics, we then move on to discuss our 2D models to study how nuclear burning interacts with multi-D hydrodynamics.

This paper opens with the description of numerical setup including information about our hydrodynamic code with nuclear network and about initial models (Section 2). Results are given in section 3. We summarize our results and discuss their implications in Section 4.

2. Numerical Setup

2.1. Hydrodynamics with Nuclear Network

We solve the hydrodynamic equations corresponding to the conservation of mass, momentum, and energy,

$$\frac{d\rho}{dt} + \rho \nabla \cdot \mathbf{v} = 0, \quad (1)$$

$$\rho \frac{d\mathbf{v}}{dt} = -\nabla p - \rho \nabla \Phi, \quad (2)$$

$$\frac{\partial e}{\partial t} + \nabla \cdot [(e + p)\mathbf{v}] = -p\mathbf{v} \cdot \nabla \Phi + \rho(H - C + Q), \quad (3)$$

where ρ is the mass density, \mathbf{v} the fluid velocity, p the pressure, Φ the gravitational potential, and e the total energy density, respectively. The Lagrangian derivative is denoted by $d/dt \equiv \partial/\partial t + \mathbf{v} \cdot \nabla$. To treat Newtonian self-gravity, a monopole approximation is employed. The tabulated realistic equation of state based on the relativistic mean field theory (Shen et al. 1998) is implemented according to the prescription in Kotake et al. (2003).

In this study, we employ the so-called light-bulb scheme (Janka & Müller 1996), in which neutrino heating and cooling is adjusted parametrically to trigger explosions. Following Janka (2001) and Nordhaus et al. (2010), the neutrino heating (H) and cooling rates (C) are given by,

$$H = 1.544 \times 10^{20} \left(\frac{L_{\nu_e}}{10^{52} \text{ erg s}^{-1}} \right) \left(\frac{T_{\nu_e}}{4 \text{ MeV}} \right)^2 \times \left(\frac{r}{100 \text{ km}} \right)^{-2} (Y_n + Y_p) e^{-\tau_{\nu_e}} [\text{erg/g s}], \quad (4)$$

$$C = 1.399 \times 10^{20} \left(\frac{T}{2 \text{ MeV}} \right)^6 (Y_n + Y_p) e^{-\tau_{\nu_e}}, [\text{erg/g s}], \quad (5)$$

where L_{ν_e} is the electron-neutrino luminosity that is assumed to be equal to the anti-electron neutrino luminosity ($L_{\bar{\nu}_e} = L_{\nu_e}$), T_{ν_e} is the electron neutrino temperature assumed to be kept constant as 4 MeV, r is the distance from the center, T is the local fluid temperature, Y_n and Y_p are the neutron and proton fractions, and τ_{ν_e} is the electron neutrino optical depth that we estimate according to Eq. (7) in Hanke et al. (2011).

Note in this study that neutrino luminosity is assumed to evolve exponentially with time (Kifonidis et al. 2003) as

$$L_{\nu_e} = L_{\bar{\nu}_e} = L_{\nu 0} \exp(-t_{\text{pb}}/t_d), \quad (6)$$

where $L_{\nu 0}$ denotes the initial luminosity, t_{pb} is the time measured after core bounce t_d is the decay time, respectively. $L_{\nu 0}$ and t_d are treated as free parameters. Note that neutrino heating and cooling are switched on only after core bounce.

We are keeping track of 13 species of α network (from ^4He to ^{56}Ni) by solving a separate advection equation for each species. Q in Eq. (3) denotes the net energy deposition rate by nuclear burning. The nuclear reaction network is mainly based on the REACLIB database (Rauscher & Thielemann 2000). Experimentally determined masses (Audi & Wapstra 1995) and reactions (Angulo et al. 1999) are adopted if available. It should be noted that our network does not include the photodissociation of iron elements because Shen EOS adopted in this study takes account of these endothermic effects. Note also that we solve the reaction network only for the grids where $T < 5 \times 10^9$ K, assuming that above this temperature the local chemical composition is in nuclear statistical equilibrium (NSE).

Only after core bounce, neutrino heating and cooling is switched on, according to the prescriptions (Equations (4) and (5)) assuming $L_{\nu_e} = L_{\bar{\nu}_e}$ and $T_{\nu_e} = T_{\bar{\nu}_e}$. Before bounce, we employ the Y_e prescription proposed by Liebendörfer (2005), in which Y_e is given simply as a function of density, and after that, we refrain from solving the change of Y_e following Murphy & Burrows (2008); Nordhaus et al. (2010) and Hanke et al. (2011) (see, however, Ohnishi et al. (2006)). As for the hydro-solver, we employ the ZEUS-MP code (Hayes et al. 2006) which has been modified for core-collapse simulations (e.g., Iwakami et al. 2008, 2009). The computational grid is comprised of 300 logarithmically spaced, radial zones to cover from the center up to 5000 km for our 1D models with 128 polar (θ) uniform mesh points for our fiducial 2D models.

In order to induce non-spherical instability after the stall of the prompt bounce shock, we have added a radial velocity perturbation, $\delta v_r(r, \theta, \phi)$, to the steady spherically symmetric flow according to the following equation,

$$v_r(r, \theta, \phi) = v_r^0(r) + \delta v_r(\theta, \phi), \quad (7)$$

with

$$\delta v_r = 0.01 \times \text{rnum} \times v_r^0(r, \theta), \quad (8)$$

where $v_r^0(r, \theta)$ is the unperturbed radial velocity and δv_r is the random multi-mode perturbation with a random number $-1 < \text{rnum} < 1$.

2.2. Progenitor models

In this study, we employ four progenitor models; three for $15.0 M_\odot$ stars of Limongi & Chieffi (2006, hereafter LC15), Woosley & Weaver (1995, WW15), and Woosley et al. (2002, WHW15)

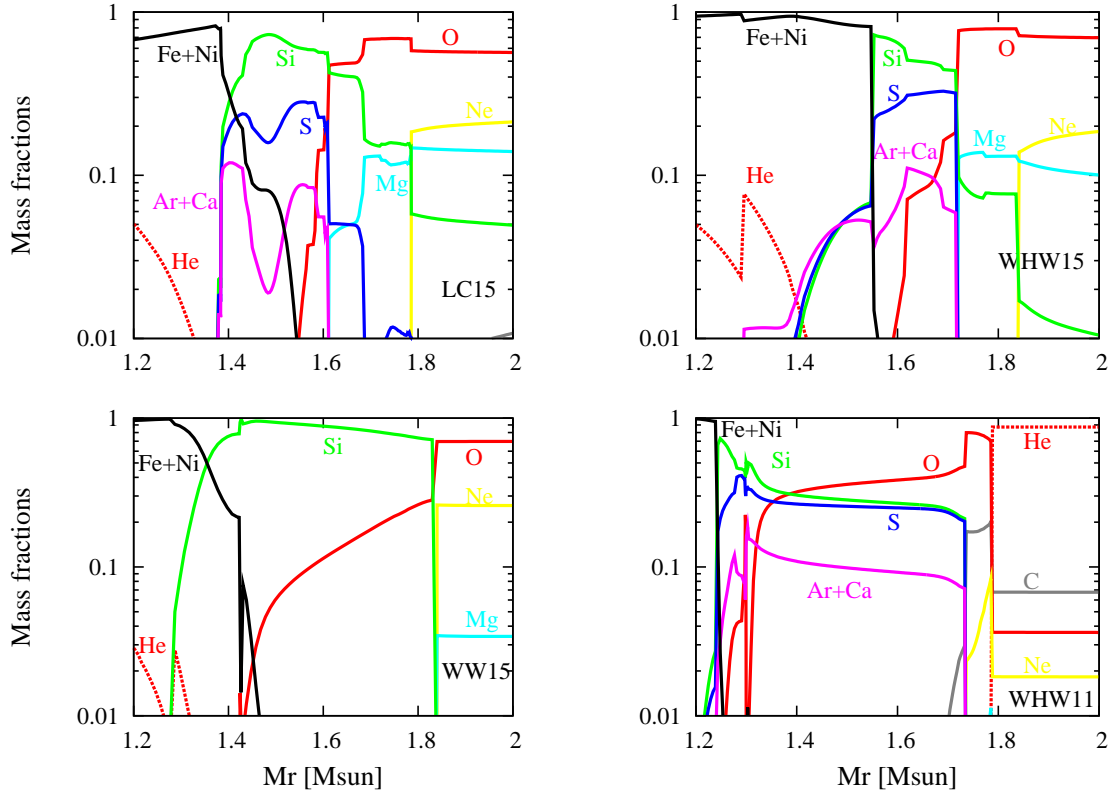


Fig. 1.— Precollapse composition distributions for the $15 M_{\odot}$ stars of Limongi & Chieffi (2006) (labeled by LC15, *top left*), Woosley & Weaver (1995) (WW15, *bottom left*), and Woosley et al. (2002) (WHW15, *top right*) and for the $11.2 M_{\odot}$ star of Woosley et al. (2002) (WHW11, *bottom right*).

and one for an $11.2 M_{\odot}$ star of Woosley et al. (2002, WHW11). For all the models, Figure 1 shows the precollapse composition profiles near from the outer edge of the iron core to outside. As we will explain in the next section, burning of the oxygen shell behind the (weakly propagating) shock plays an important role in assisting the shock expansion. Therefore, the earlier the oxygen layer touches the (stalling) shock after bounce, the better it could work. Having this in mind, let’s see Figure 1 again. Among the three variants of the $15 M_{\odot}$ progenitors, the inner edge of the oxygen layer (seen as a sharp decline in solid red lines of Figure 1) is positioned much closer to the center for models LC15 (closest, top left panel) and WHW15 (next closest, top right panel) compared to model WW15 (bottom left panel). Table 1 shows a summary of the precollapse abundance distributions, in which each quantity from the left to right column corresponds to the different progenitor models, the progenitor mass, the mass of the iron core, the outer edge of the iron core, the mass of the silicon layer, the outer edge of the silicon layer, and the mass of the oxygen layer, respectively. The edge between each layer is defined as the radius where the most abundant element shifts to one another (see, Figure 1). The mass of oxygen layer for the $15 M_{\odot}$ models of LC15 and WHW15 (M_O in the table) is larger than the other progenitors (i.e., WW15 and WHW11) and their oxygen layers (denoted by $R_{\text{Si/O}}$) are positioned much closer to the center, so that they can touch to the supernova shock in a shorter timescale after bounce (before the neutrino luminosity gets smaller with time). As one would anticipate, the impacts of nuclear burning are most remarkable for the LC15 progenitor as we will show in the later sections.

Table 1: Summary of progenitor models and their composition features (see text for the definition of each quantity).

Model	M_{total} (M_{\odot})	M_{Fe} (M_{\odot})	$R_{\text{Fe/Si}}$ (10^3 km)	M_{Si} (M_{\odot})	$R_{\text{Si/O}}$ (10^3 km)	M_O (M_{\odot})
LC15	13.4	1.44	1.31	0.221	2.22	0.814
WHW15	12.6	1.55	1.96	0.124	2.97	0.943
WW15	15.0	1.42	1.31	0.436	7.44	0.649
WHW11	10.8	1.24	1.00	0.168	3.74	0.289

3. Results

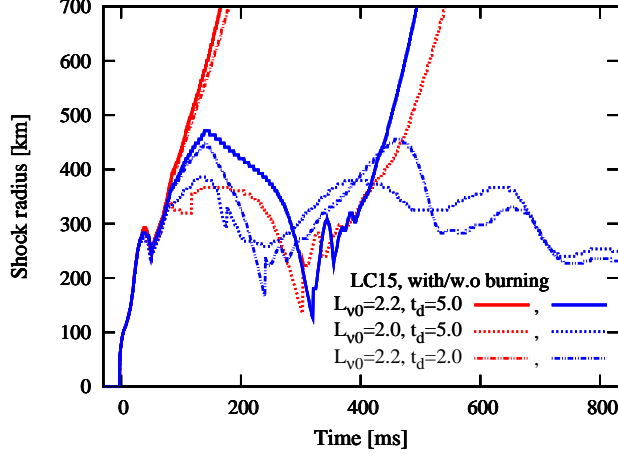


Fig. 2.— Time evolution of the shock radii for model LC15 with different initial neutrino luminosities ($L_{\nu 0,52}$ in unit of 10^{52} erg s $^{-1}$) and the decay time (t_d in unit of s). The red and blue line corresponds to the results with and without the energy feedback from nuclear reactions, respectively.

In section 3.1, we start to investigate how the energy feedback from nuclear burning could affect the postbounce dynamics in 1D simulations. Then we study how the nuclear-burning impacts are sensitive to the progenitor models, namely by the precollapse structures and their composition profiles (section 3.2). In section 3.3, we then move on to discuss how nuclear burning would affect the 2D dynamics.

3.1. Impact of Nuclear Burning in 1D simulations

Relying on the light-bulb scheme in this study, the destiny of the stalling bounce shock (whether it will revive or not) depends simply on the two parameters; the input neutrino luminosity $L_{\nu 0}$ and the decay time t_d (see Equation (6))⁴. Note in the following that we characterize models as $(L_{\nu 0,52}, t_d) = (x, y)$ for convenience, in which the luminosity and the decay time is $x \times 10^{52}$ (erg/s) and y (s), respectively. Figure 2 shows comparisons of the postbounce shock evolution in 1D LC15 models depending on the two parameters with (red lines) or without (blue lines) the α network calculation.

⁴Without seeing a shock revival in ~ 1 s postbounce, we call it as "non-exploding" in this study

For the chosen three cases in the figure; $(L_{\nu 0,52}, t_d) = (2.2, 5.0)$ (solid line), $(2.0, 5.0)$ (dotted line), and $(2.2, 2.0)$ (dashed line), all of the models with nuclear burning (red lines) show a shock expansion leading to explosions finally, while among the models without nuclear burning the solid blue line only exhibits a shock revival. This is the case of relatively higher luminosity with longer decay time ($(L_{\nu 0,52}, t_d) = (2.2, 5.0)$). Note that in all the six cases (3 different parameters $\times 2$ (with/without burning)) in Figure 2, the bounce shock firstly stalls and then transits to a passive shock with no positive velocity (seen as a shrink of the shock radii at around ~ 50 ms postbounce in Figure 2). And only after that, the additional energy gain due to nuclear burning acts to bifurcate the path of the passive shock, namely whether the shock experiences recession afterward (for all the blue lines in Figure 2) or expansion (for red lines) with different revival timescales depending on the input neutrino parameters.

As seen from Figure 2, larger input neutrino luminosity and shorter decay timescale (unsurprisingly) lead to more easier explosions. More importantly, by comparing dotted red with dotted blue line ($(L_{\nu 0,52}, t_d) = (2.0, 5.0)$), the shock is shown to shift from recession to expansion by the inclusion of nuclear burning. In the case of more luminous neutrino ($L_{\nu 0,52} = 2.2$), the trajectories of the shock are observed to be rather similar when the effect of nuclear burning is taken into account (compare solid red with dashed red line).

In the following, we elaborate on how and why the shock expansion is affected by nuclear burning as observed in Figure 2. Figure 3 and 4 show the mass-shell trajectory of models LC15 with the different parameter set of $(L_{\nu 0,52}, t_d) = (2.2, 2.0)$ and $(L_{\nu 0,52}, t_d) = (2.0, 5.0)$, respectively. Note here that the former and latter case corresponds to the dashed and dotted line in Figure 2. Without nuclear burning (left panels in Figure 3 and 4), the stalled shock, albeit showing several oscillations, does not turn into expansion (see also Figure 2). With nuclear burning, by looking carefully at the right panels of Figures 3 and 4, the shock expansion can be seen to take place in the following two ways, whether the shock front passes through the Si-rich layer (see the behavior of the thick red line in the greenish region in the right panel of Figure 3) or later it touches to the O-rich layer (e.g., the shock in the reddish region in the right panel of Figure 4). For the latter case, the bounce shock firstly stalls as in the non-burning model (compare the left with the right panel in Figure 4), but then the shock front says good-bye to the non-burning case when it encounters with the O-rich layer.

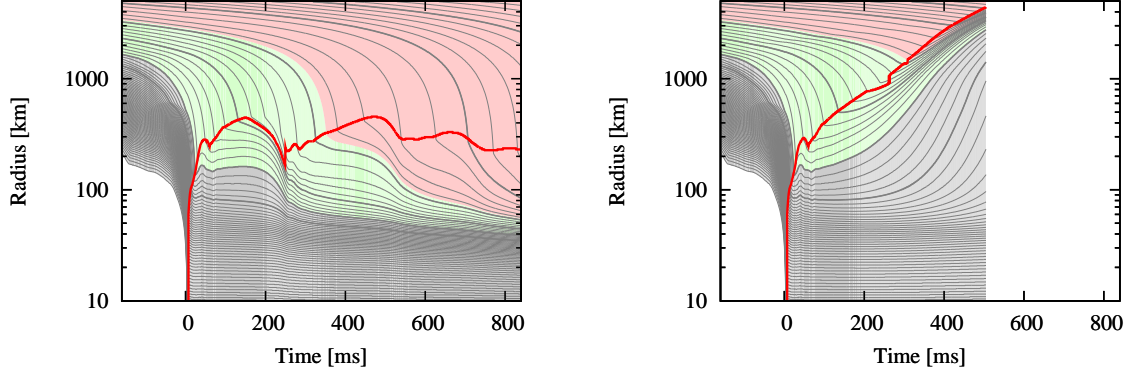


Fig. 3.— Evolution of model LC15 with a parameter set of $(L_{\nu 0,52}, t_d) = (2.2, 2.0)$ visualized by the mass-shell trajectories. The thick red line starting at $t = 0$ denotes the position of the shock. Both cases either without (*left*) or with (*right*) the energy feedback from nuclear reactions are shown. The regions colored by gray, green, and red correspond to the iron, silicon, and oxygen layers, respectively. Thick gray lines correspond to the mass coordinates from 1.3 to $1.8 M_{\odot}$ with every $0.1 M_{\odot}$ (thin gray lines with every $0.02 M_{\odot}$).

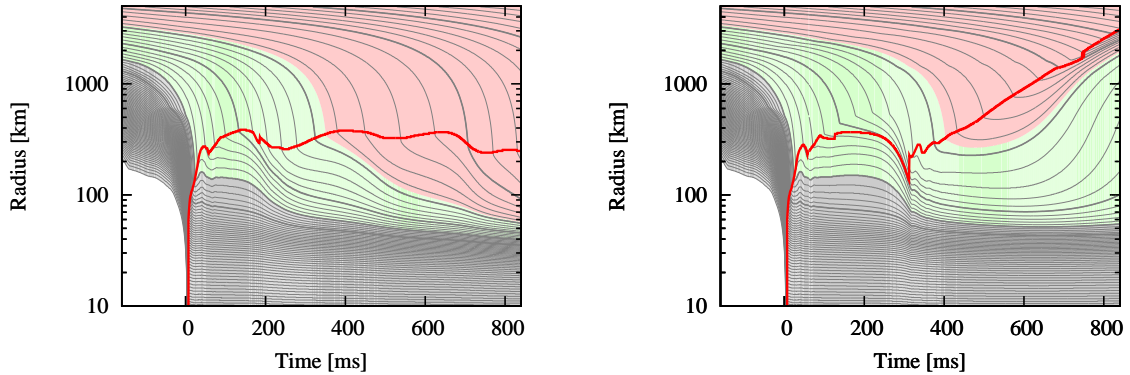


Fig. 4.— Same as Figure 4 but for the parameter set of $(L_{\nu 0,52}, t_d) = (2.0, 5.0)$.

To look more in detail how the nuclear burning contributes to the shock acceleration, Figure 5 shows the radial velocity profiles and the composition distributions for model LC15 with the parameter set of $(L_{\nu 0,52}, t_d) = (2.2, 2.0)$ (the same parameter set as in Figure 3). At $t_{\text{pb}} = 150$ ms (top left panel), the shock front is in the silicon-rich layer (seen as a rapid decline of the green line in the mass fraction plot). Behind the shock front, heavier elements are synthesized as shown. The nuclear energy released by the silicon burning heats the material behind the shock, making the sign of the velocity slightly positive there (compare the velocity profiles with and without nuclear burning in the top left panel). The difference between the velocity profiles with versus without nuclear burning becomes outstanding when the oxygen-rich layer starts to touch the shock front ($t_{\text{pb}} > 250$ ms). The left panel of Figure 6 shows the evolution of the explosion energy with (red line)/without (blue line) burning and also that of the net energy released via nuclear reactions (green line). After the silicon burning starts to feed the energy behind the shock in addition to the neutrino heating (in the gain region, e.g., $t_{\text{pb}} = 150$ ms, see the top left panel in Figure 5), the explosion energy deviates from the one without burning (compare red with blue line in the left panel in Figure 6), which is also clearly visible in the shock evolution (compare red with blue line in the right panel in Figure 6). From the left panel of Figure 6, the total amount of 3.1×10^{50} erg is shown to be released through nuclear burning in this case, lifting up the explosion energy to be 5.0×10^{50} erg.

As we already mentioned, the oxygen burning predominantly triggers the shock expansion for the parameter set taken for Figure 4. But also in this case, the silicon layer is shown to be burned as a heating source (top left panel of Figure 7), which is the reason that the shock position becomes larger compared to the non-burning model (see the right panel of Figure 8). When the shock front begins to swallow the oxygen layer at ~ 400 ms postbounce (the right panel of Figure 4), the fresh fuel supplies energy to assist the shock expansion (see, from top right, bottom left, to bottom right panels of Figure 7). If not for the energy gain, the stalled shock does not revive no earlier than $t = 750$ ms as seen from the right panel of Figure 8. Even with the aid of nuclear burning, the explosion for this model (left panel of Figure 8) is weaker ($\lesssim 10^{50}$ erg) comparing to the more luminous models (left panels of Figures 6 and 9). This suggests that nuclear burning has a secondary impact on the explosion mechanism in the sense that it can assist explosions only when the neutrino heating is working enough strong to push the weak shock to the fuel layers.

In this section, we have elaborated on the features of the burning affects by taking the three different models as a reference. In the next section, we proceed to study a systematic trend by showing the parameter region spanned by $L_{\nu 0}$ and t_d (as well as its progenitor dependence), where nuclear burning is able to affect the neutrino-driven explosions.

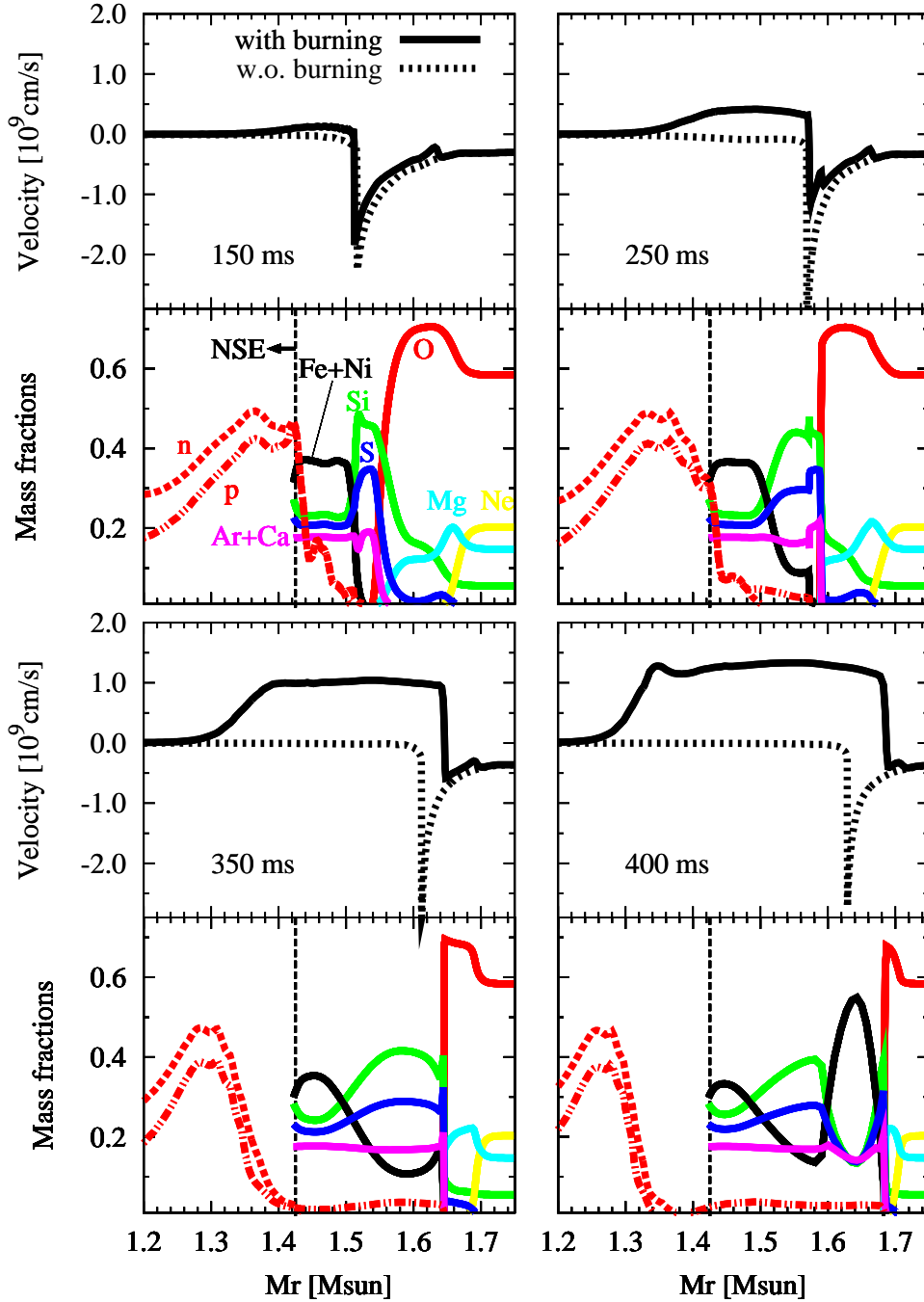


Fig. 5.— Snapshots of velocity profile (*top*) and composition distribution (*bottom*) for model LC15 with $L_{\nu,0} = 2.2 \times 10^{52} \text{ erg s}^{-1}$ and $t_d = 2.0 \text{ s}$ at selected postbounce epochs ($t_{\text{pb}} = 150, 250, 350,$ and 400 ms). Solid and dotted line in the top of each panel shows the velocity profile with or without nuclear burning, respectively. In the bottom part, distributions of representative elements are shown. Note that the abundances of neutron (n) and proton (p) in the NSE core (regions below the horizontal dashed line in the abundance plot) are estimated from Shen’s EOS and the abundances of the other elements outside are calculated from the nuclear network calculation.

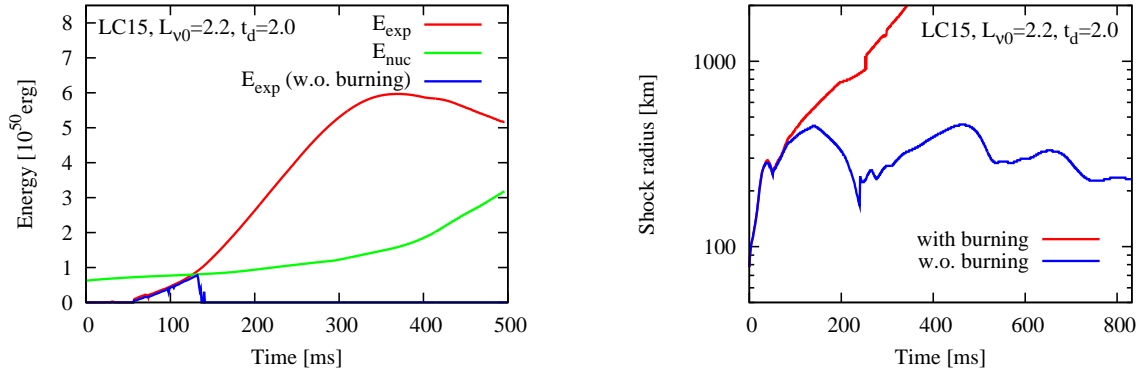


Fig. 6.— For the same model as Figure 5, the evolution of explosion energy (*left*) and the shock radius (*right*) are shown, respectively. In the left panel, the green line is the energy released by the nuclear burning and the explosion energy without nuclear burning (*blue*) is also shown. Here the explosion energy is defined as the sum of the kinetic, thermal, and gravitational energy of fluid elements with positive radial velocity.

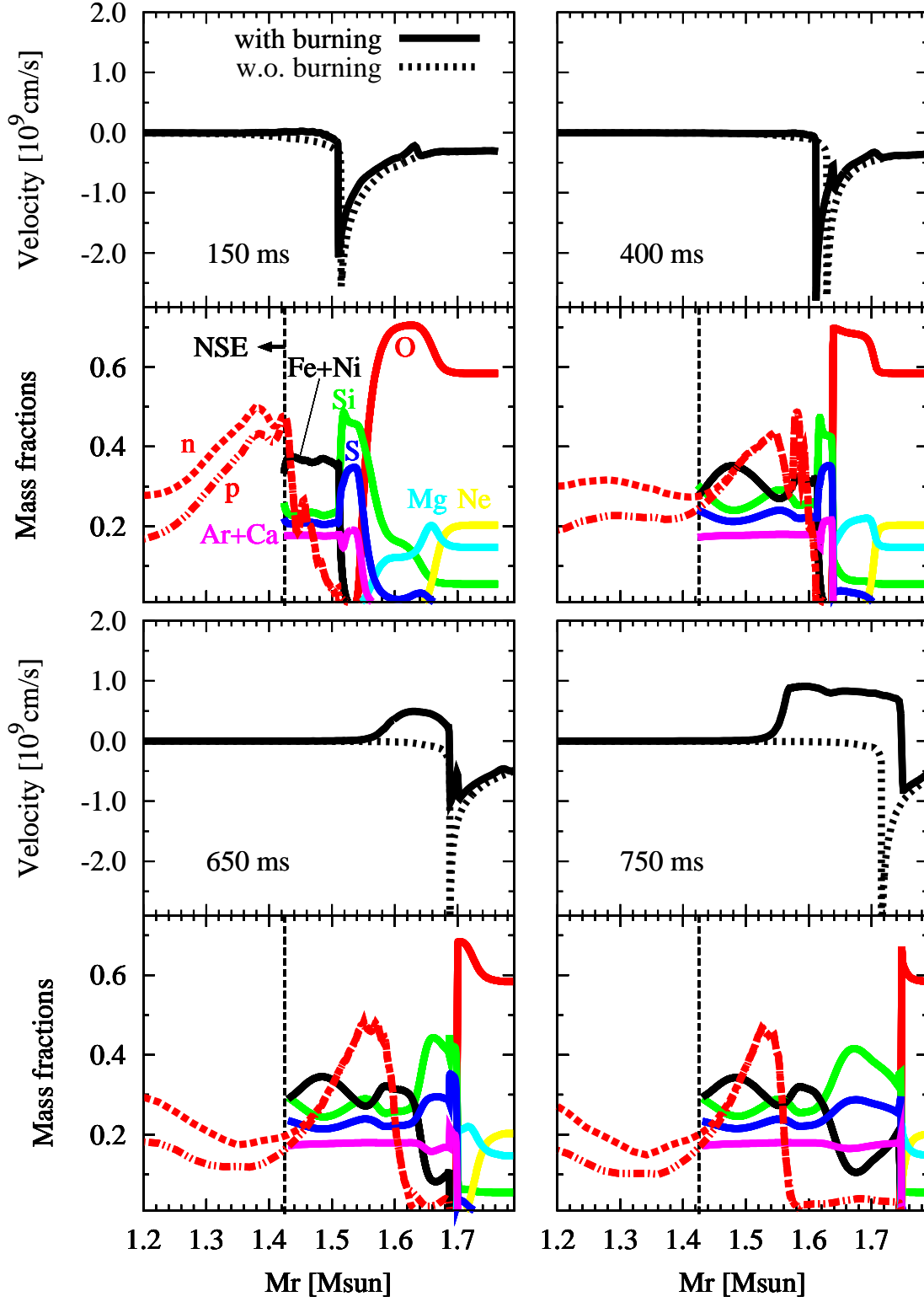


Fig. 7.— Same as Figure 5 but for the parameter set of $L_{\nu 0} = 2.0 \times 10^{52}$ erg/s and $t_d = 5.0$ s.

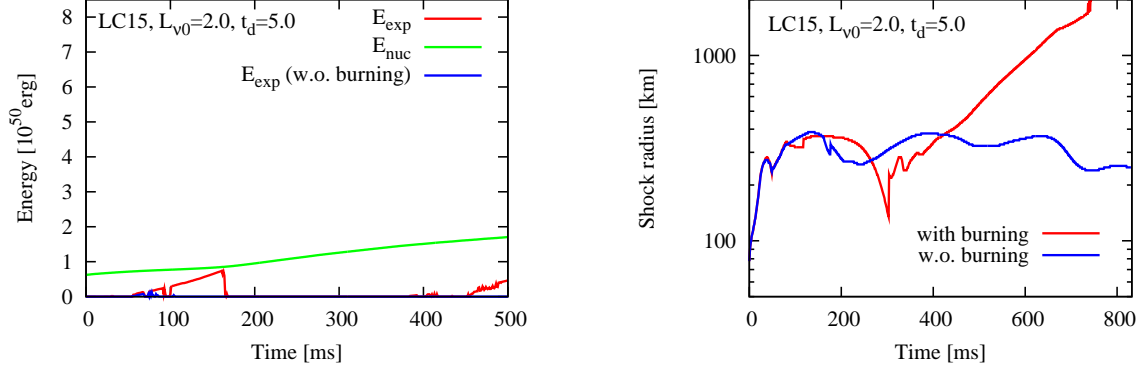


Fig. 8.— Same as Figure 6 but for the parameter set of $L_{\nu 0} = 2.0 \times 10^{52}$ erg/s and $t_d = 5.0$ s.

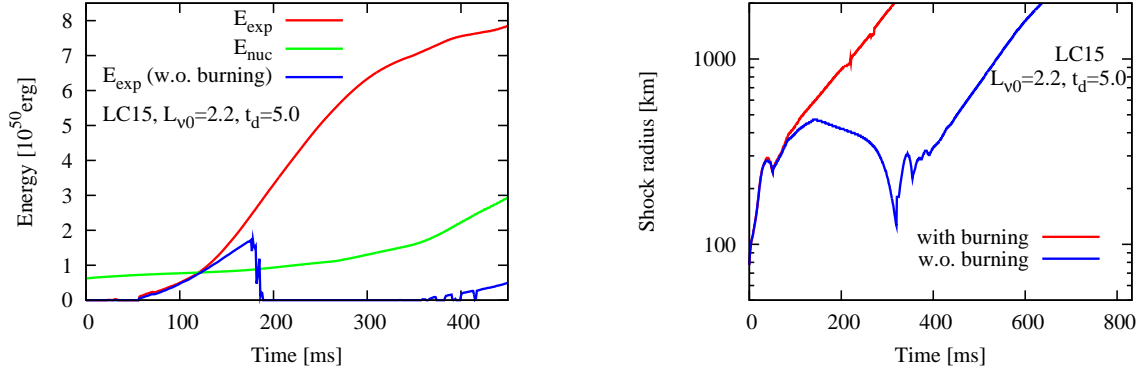


Fig. 9.— Same as Figure 6 but for the most energetic case, $(L_{\nu 0, 52}, t_d) = (2.2, 5.0)$, among the three examples shown in Figure 2. The explosion energy with nuclear burning is about 8.0×10^{50} ergs at $t_{pb} = 465$ ms and still keeps rising. The net energy released via nuclear reactions at this time is $\sim 3.0 \times 10^{50}$ erg, occupying a significant fraction ($\sim 40\%$) of the explosion energy. For the model without nuclear burning, the explosion energy is $\sim 0.8 \times 10^{50}$ erg at that time and closely saturates to be $E_{\text{exp}} \sim 2.3 \times 10^{50}$ erg afterward.

3.2. Progenitor Dependence

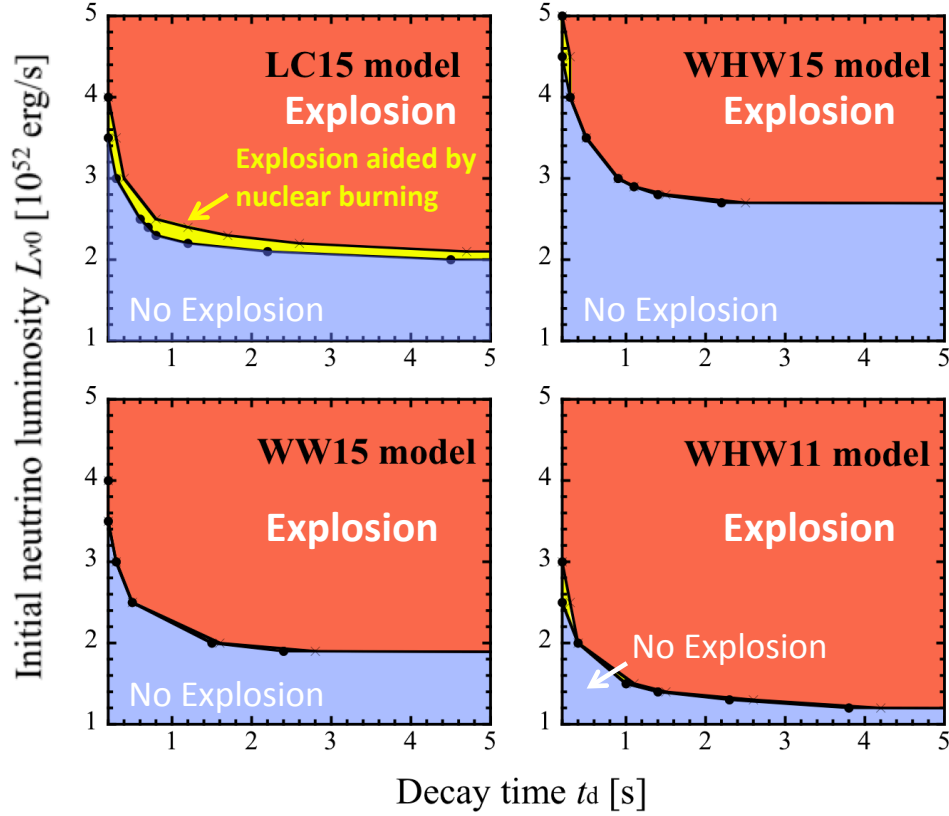


Fig. 10.— Parameter maps of the initial neutrino luminosity ($L_{\nu 0}$) and its decay time (t_d) that separates the non-exploding regime (blueish region) from the exploding one (reddish regime) in 1D simulations for the four different progenitors. A horizontal yellowish region in-between (clearly visible for the LC15 progenitor; *top left*) shows the parameter region in which 1D explosions are obtained when the network calculation is performed.

Figure 10 shows the parameter region on the $(L_{\nu 0}, t_d)$ plane, in which 1D explosions are obtained only if the network calculation is performed (the yellowish region sitting between the exploding and the non-exploding regime). The burning-mediated regime is clearly visible only for the LC15 progenitor. As already mentioned in section 2.2, this is because this model possesses a massive oxygen layer and the oxygen shell is positioned closest to the center among the progenitors taken in this study.

The area of the yellowish region in Figure 10 is not so big even for the LC15 progenitor, which suggests again that nuclear burning has a secondary importance because it can work

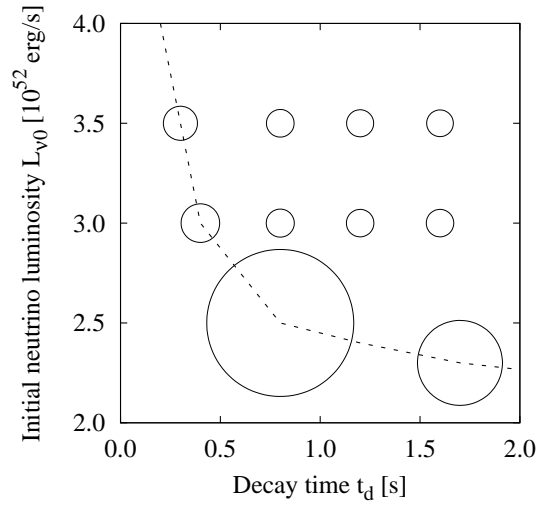


Fig. 11.— Ratio of the explosion energy with nuclear burning to that without for model LC15 on the $(L_{\nu 0}, t_d)$ plane. The dashed line is the boundary between the exploding and the "nuclear-burning-aided" regime in Figure 10. In this plot, the radius of each circle is taken to be proportional to the ratio of the explosion energy, where the ratio (the size of the circle) becomes smaller to be approaching to unity for models with higher input luminosity and with longer decay time (from lower left to upper right direction in this map).

only when the neutrino-driven explosion takes place very marginally. In the case of the marginal explosions (which may be often the case in recent first-principle CCSN simulations), however, it should be emphasized that the inclusion of nuclear burning does lead to the enhancement of the explosion energy. Figure 11 shows the ratio of the explosion energy with nuclear burning to that without for model LC15 on the $(L_{\nu 0}, t_d)$ plane. In fact, the explosion energy is shown to be remarkably enhanced in the case of marginal explosions (i.e., the size of the circle becomes larger on the critical curves (dashed line)), and getting small for large $L_{\nu 0}$ and t_d , in which explosions are predominantly triggered by neutrino heating. As repeatedly mentioned so far, these features due to nuclear burning are only remarkable in the LC15 progenitor. Nevertheless, it is worth mentioning that the shock extent even for the WW95 progenitor (which is the most pessimistic case, see the bottom left panel of Figure 10) becomes bigger for models with nuclear burning compared to those without (Figure 12).

The critical luminosity for explosions can be read from the y -axis in Figure 10 in the limit of long t_d (namely, approaching to a constant neutrino luminosity), which corresponds to 2.7 (WHW15), 2.0 (LC15), 1.9 (WW15), and 1.2 (WHW11) in unit of 10^{52} erg/s, respectively. The critical luminosity becomes smallest for model WHW11 (mainly due to a compactness of the precollapse core and its tenuous envelope). When the input luminosity is taken below the critical curves, nuclear burning cannot alone drive explosions because the shock needs to be kicked out of the iron core firstly by neutrino heating (i.e., the shock revival due to neutrino heating is preconditioned to enjoy the assistance from nuclear burning).

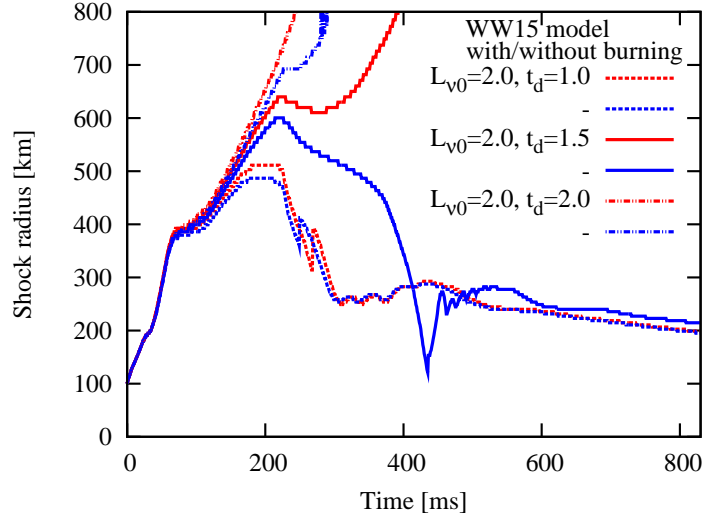


Fig. 12.— Time evolution of the shock radii for several 1D models employing the WW15 progenitor. The shock moves farther out for models including nuclear burning (red lines) compared to those without (blue)

3.3. 2D Results

To see clearly the impacts of nuclear burning in our 2D simulations, we choose to employ the LC15 in the following.

Figures 13 and 14 show entropy evolution (left-hand-side in the left panel) with the abundances of representative elements of oxygen, silicon, and nickel (from the right-hand-side in the left panel to the right-hand-side in the right panel) for two sets of neutrino parameters at selected postbounce epochs ($t_{\text{pb}} = 100(\text{top})$, $200(\text{middle})$ and $300(\text{bottom})$ ms postbounce), respectively. Small- and large-scale inhomogeneities in the entropy plots come from neutrino-driven convection and the SASI, both of which lead to more easier explosions in 2D than 1D (e.g., Marek & Janka 2009; Ohnishi et al. 2006; Murphy & Burrows 2008).

Reflecting the stochastic motions of the expanding shocks, the way how the (anisotropic) shock surfaces touch the nuclear fuel (in the shape of spherical shells) changes from models to models in 2D. In the case of Figure 13, the anisotropically expanding shock firstly reaches to the oxygen layer near in the vicinity of the north pole at $t \sim 200$ ms, which is seen as a penetration of the blueish region to the reddish region there (;oxygen layer (*middle left*)). Simultaneously, heavy elements like silicon and nickel are shown to be synthesized there (*middle right*), which helps to push the burning material preferentially along the direction for the moment (see the reddish region of the nickel abundance in the bottom right panel). In a more luminous case assuming larger luminosity and longer decay time (Figure 14), the SASI seemingly develops only weakly, barely deforming the the shock surface (essentially spherical), although neutrino-driven convection does make the postshock entropy distribution non-uniform.

As shown from Figure 15, nuclear burning does assist 2D explosions similar to 1D, but the energy difference (here $\sim 0.2 \times 10^{51}$ erg) is generally smaller in 2D than in 1D (compare with Figures 6, and 9). The comparison of the energy gain due to nuclear burning between 1D and 2D models is more clearly shown in Figure 16. In the figure, the difference of the explosion energy (ΔE_{exp}) with and without nuclear burning is shown as a function of the mass of the oxygen layer that is burned due to the shock passage ($M_{\text{O,brn}}$) both in 1D (open circles) and 2D (closed circles) models for the LC15 progenitor. The slope of ΔE_{exp} as a function of $M_{\text{O,brn}}$ is shown to be milder in 2D than in 1D. This may be because neutrino-driven convection and the SASI in 2D models (as indicated by entropy distributions in Figures 13 and 14) could enhance the neutrino heating efficiency, which makes the contribution of nuclear burning relatively smaller compare to 1D models.

Finally Figure 17 shows a parameter map in 2D for the LC15 progenitor (compare Figure 10 in 1D). As expected, 2D hydrodynamics leads to more easier explosions compared

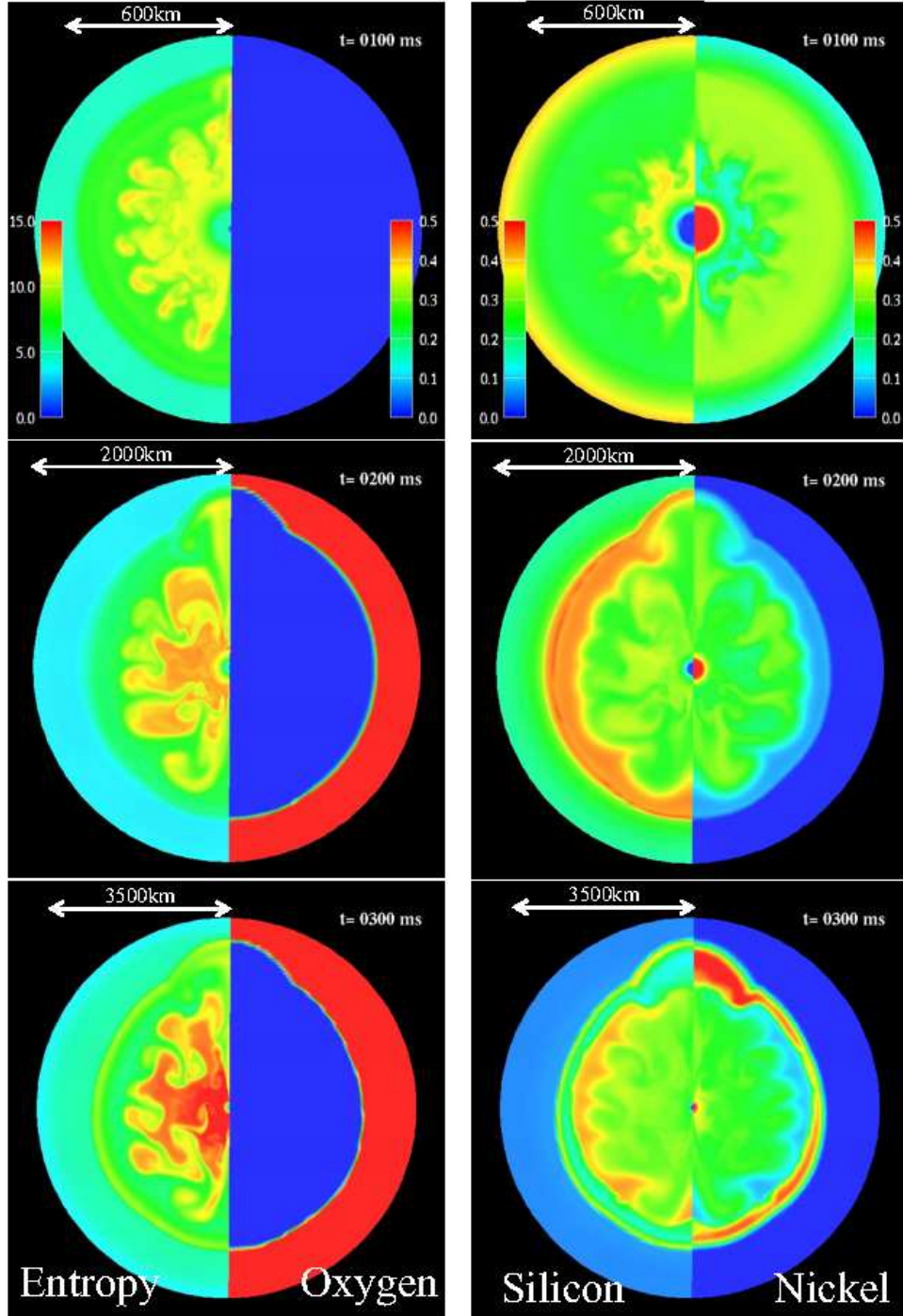


Fig. 13.— 2D distributions of entropy and representative elements (O, Si, and Ni) of model LC15 for $(L_{\nu 0,52}, t_d) = (2.7, 1.1)$ at $t_{\text{pb}} = 100$ (*top*), 200 (*middle*), and 300 ms (*bottom*) postbounce, respectively. In this case, the anisotropically expanding shock firstly reaches to the oxygen layer near in the vicinity of the north pole at $t \sim 200$ ms, which is seen as an aspherical penetration of the blueish region to the oxygen layer (reddish region (*left*)). Looking at the corresponding region in the middle right panel, heavy elements like silicon and nickel are shown to be synthesized.

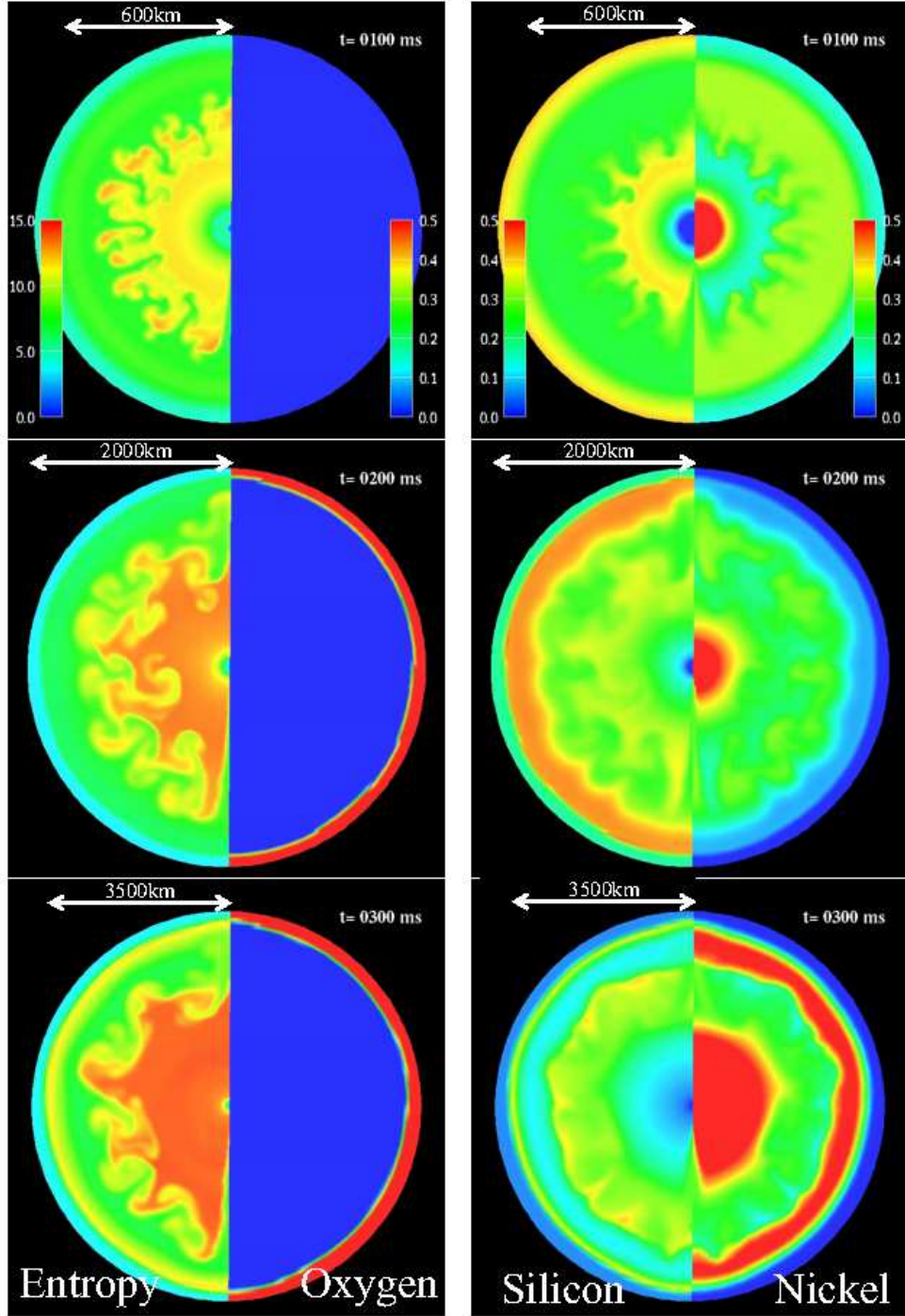


Fig. 14.— Same as Figure 13 but of a 2D model with $(L_{\nu 0,52}, t_d) = (3.0, 1.1)$. In this case neutrino irradiation is very strong and its effective heating leads to nearly spherical shape.

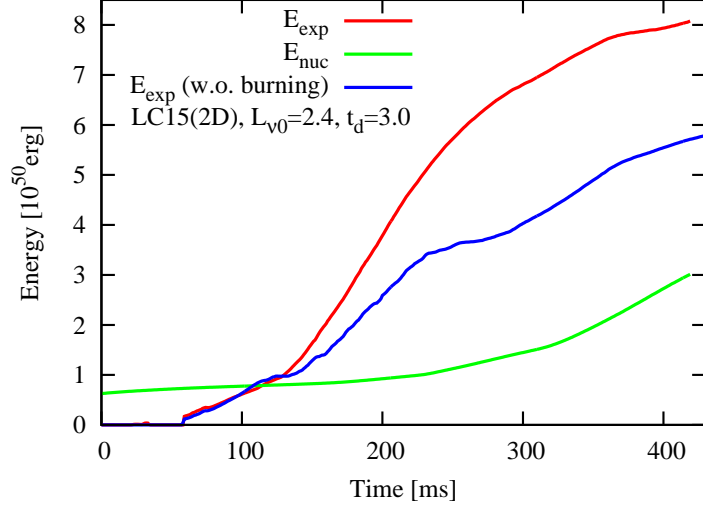


Fig. 15.— Time evolution of explosion energy (*red line*) and net nuclear burning energy (*green*) for LC15 model with $L_{\nu,0} = 2.4$ and $t_d = 3.0$. Explosion energy of the case without nuclear burning (*blue*) is also shown.

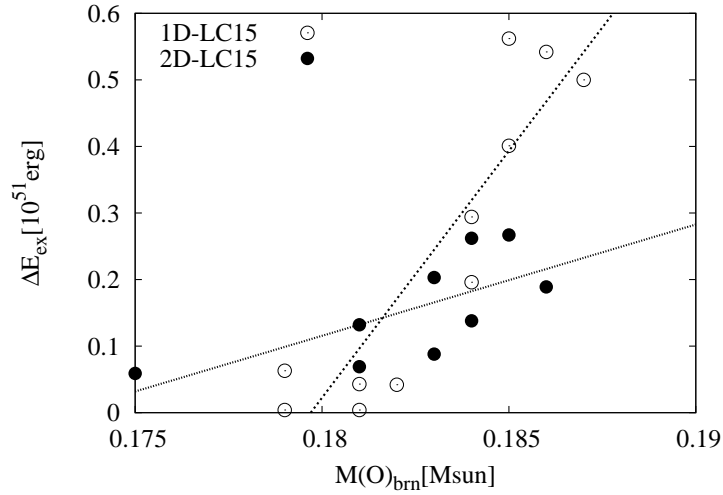


Fig. 16.— Shown is the differences of explosion energy between models including and not including the effects of nuclear burning as functions of the consumed mass of oxygen. Results from spherical (*open circles*) and 2-dimensional (*filled*) simulations for LC15 model are plotted. Lines are for linear fit of both data.

to 1D (see the dotted lines which are the critical curves in 1D). More importantly, the yellowish region does form in 2D models for the LC15 progenitor. It should be interesting to perform multi-D (radiation-hydro) simulations with nuclear network calculation for the virgin progenitor model. Given a number of uncertainties in the pre-supernova evolution calculations (such as in treatments of multi-D effects, mass-loss, and weak interactions), our results would indicate that the consideration of nuclear burning remains as one of the unignorable ingredients in the first-principle simulations as a potential remedy to cure these underpowered symptoms.

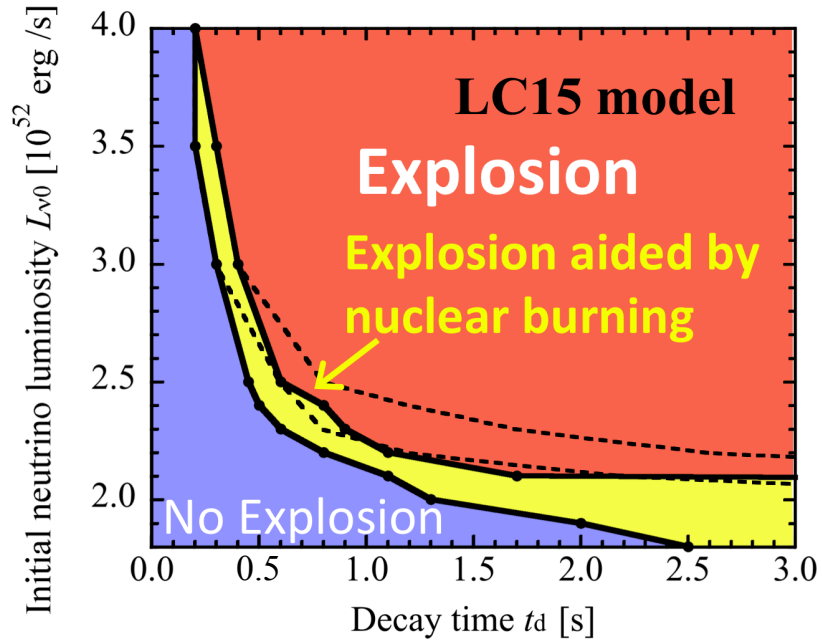


Fig. 17.— Same as Figure 10 but for 2D simulations. The dashed lines represent the critical curves in 1D (compare Figure 10). Note that we adopt coarse mesh points in the polar direction (32 uniform grids), so that we can perform 2D simulations for 174 models in total to make this parameter map.

4. Conclusion

We explored the potential impacts of nuclear burning on fostering the onset of the neutrino-driven explosions of core-collapse supernovae. By changing the neutrino luminosity and its decay time to obtain parametric explosions in 1D and 2D models with or without a

^{13}C -isotope α network, we studied how the inclusion of nuclear burning could affect the post-bounce dynamics for four progenitor models; three for $15.0 M_{\odot}$ stars of Limongi & Chieffi (2006), Woosley & Weaver (1995), and Woosley et al. (2002), and one for an $11.2 M_{\odot}$ star of Woosley et al. (2002). Our results showed that the energy gain due to nuclear burning of infalling material behind the shock can energize the shock expansion especially for models that produce only marginal explosions in the absence of nuclear burning. These models enjoy the assistance from nuclear burning typically in the following two ways, whether the shock front passes through the silicon-rich layer, or later it touches to the oxygen-rich layer. Depending on the neutrino luminosity and its decay time, the explosion energy was found to increase up to a few times 10^{50} erg for models with nuclear burning compared to the corresponding models without. The difference in the explosion energy becomes generally smaller in 2D than in 1D, because neutrino-driven convection and the SASI in 2D models enhance the neutrino heating efficiency, making the contribution of nuclear burning relatively smaller compared to 1D models. It was pointed out that these features are remarkable only for the LC15 progenitor both in 1D and 2D, which possesses a massive oxygen layer with its inner-edge radius being smallest among the employed progenitors, which makes the timescale shorter for the shock to encounter the rich fuel. Considering uncertainties in progenitor models, our results indicate that nuclear burning should still remain as one of the unignorable ingredients to foster the onset of neutrino-driven explosions.

An important extension of this study would be going to 3D simulations with the same setting. Without the coordinate symmetry axis, the anisotropy of the expanding shock is expected to be much milder in 3D than in 2D. If this would be the case, the impacts of nuclear burning in 3D could be more important than in 2D, provided that the shock morphology in 3D would be more close to that in 1D (Hanke et al. 2011). It should be interesting to employ the LC15 model, which has been unexplored by 2D and 3D radiation-hydro simulations including a network calculation. Suppose that nuclear burning impacts the explosion dynamics and its blast morphology, their consequences on the multi-messenger observables (see, Kotake et al. 2012, for a recent review) such as kick/spin of pulsars (e.g., Wongwathanarat et al. 2010) and nucleosynthetic yields (e.g., Arcones & Thielemann (2012); Fujimoto et al. (2011)) as well as neutrino and gravitational-wave signals (e.g., Marek et al. 2009; Ott et al. 2012; Lund et al. 2010; Müller et al. 2012; Kotake et al. 2009a,b, 2011, 2012) might deserve further investigation. We hope that our results would give a chance/momentum for CCSN researchers to reexamine the nuclear-burning effects on their own results.

We are grateful to T. Kuroda, Y. Suwa, T. Kajino for helpful exchanges. KK and TT are thankful to S. Yamada and K. Sato for continuing encouragements. Numerical computations were carried out in part on XT4 and general common use computer system at the center

for Computational Astrophysics, CfCA, the National Astronomical Observatory of Japan. This study was supported in part by the Grants-in-Aid for the Scientific Research from the Ministry of Education, Science and Culture of Japan (Nos. 20740150, and, 23340069, 23540323) and by HPCI Strategic Program of Japanese MEXT.

REFERENCES

- Angulo, C., Arnould, M., Rayet, M., Descouvemont, P., Baye, D., Leclercq-Willain, C., Coc, A., Barhoumi, S., Aguer, P., Rolfs, C., Kunz, R., Hammer, J. W., Mayer, A., Paradellis, T., Kossionides, S., Chronidou, C., Spyrou, K., degl’Innocenti, S., Fiorentini, G., Ricci, B., Zavatarelli, S., Providencia, C., Wolters, H., Soares, J., Grama, C., Rahighi, J., Shotton, A., & Laméhi Rachti, M. 1999, *Nuclear Physics A*, 656, 3
- Arcones, A., & Thielemann, F.-K. 2012, arXiv:1207.2527
- Arcones, A., Martínez-Pinedo, G., O’Connor, E., Schwenk, A., Janka, H.-T., Horowitz, C. J., & Langanke, K. 2008, *Phys. Rev. C*, 78, 015806
- Audi, G. & Wapstra, A. H. 1995, *Nuclear Physics A*, 595, 409
- Bethe, H. A. & Wilson, J. R. 1985, *ApJ*, 295, 14
- Blondin, J. M., Mezzacappa, A. & DeMarino, C., 2003, *ApJ*, 584, 971
- Bruenn, S. W., Mezzacappa, A., Hix, W. R., Blondin, J. M., Marronetti, P., Messer, O. E. B., Dirk, C. J., & Yoshida, S. 2010, ArXiv e-prints
- Bruenn, S. W., Dirk, C. J., Mezzacappa, A., Hayes, J. C., Blondin, J. M., Hix, W. R., & Messer, O. E. B. 2006, *Journal of Physics Conference Series*, 46, 393
- Buras, R., Rampp, M., Janka, H.-Th. & Kifonidis, K., 2006a, *A&A*, 447, 1049
- Buras, R., Janka, H.-Th., Rampp, M. & Kifonidis, K., 2006b, *A&A*, 457, 281
- Burrows, A., & Goshy, J. 1993, *ApJ*, 416, L75
- Burrows, A., Hayes, J. & Fryxell, B. A., 1995, 450, 830
- Burrows, A., Livne, E., Dessart, L., Ott, C. D., & Murphy, J. 2006, *Astrophys. J.*, 640, 878
- Burrows, A., Dessart, L., Livne, E., Ott, C. D., & Murphy, J. 2007a, *Astrophys. J.*, 664, 416

- Colgate, S. A. & White, R. H., 1966, *ApJ*, 143, 626
- Couch, S. M. 2012, [arXiv:1206.4724](#)
- Demorest, P. B., Pennucci, T., Ransom, S. M., Roberts, M. S. E., & Hessels, J. W. T. 2010, *Nature*, 467, 1081
- Fernández, R. & Thompson, C. 2009a, *ApJ*, 703, 1464
- . 2009b, *ApJ*, 697, 1827
- Fernández, R. 2010, *ApJ*, 725, 1563
- Foglizzo, T., Scheck, L. & Janka, H.-Th., 2006, *ApJ*, 652, 1436
- Foglizzo, T., Galletti, P., Scheck, L., & Janka, H.-T. 2007, *ApJ*, 654, 1006
- Foglizzo, T., Masset, F., Guilet, J., & Durand, G. 2012, *Physical Review Letters*, 108, 051103
- Fujimoto, S.-i., Kotake, K., Hashimoto, M.-a., Ono, M., & Ohnishi, N. 2011, *ApJ*, 738, 61
- Guilet, J., Foglizzo, T., & Fromang, S. 2011, *ApJ*, 729, 71
- Fryer, C. L. 2004, *Astrophys. J. Lett.*, 601, L175
- Fryer, C. L., Holz, D. E., & Hughes, S. A. 2002, *Astrophys. J.*, 565, 430
- Hanke, F., Marek, A., Mueller, B., & Janka, H.-T. 2011, [arXiv:1108.4355](#)
- Haxton, W. C. 1988, *Physical Review Letters*, 60, 1999
- Hayes, J. C., Norman, M. L., Fiedler, R. A., Bordner, J. O., Li, P. S., Clark, S. E., ud-Doula, A., & Mac Low, M. 2006, *ApJS*, 165, 188
- Herant, M., Benz, W. & Colgate, S., 1992, *ApJ*, 395, 642
- Iwakami, W., Kotake, K., Ohnishi, N., Yamada, S., & Sawada, K. 2008, *Astrophys. J.*, 678, 1207
- . 2009, *Astrophys. J.*, 700, 232
- Janka, H.-T. 2012, [arXiv:1206.2503](#), accepted by *Annual Review of Nuclear and Particle Science*
- Janka, H.-T., Kifonidis, K., & Rampp, M. 2001, *Physics of Neutron Star Interiors*, 578, 363

- Janka, H.-Th., 2001, A&A, 368, 527
- Janka, H.-T. & Müller, E., 1996, A&A, 306, 167
- Kifonidis, K., Plewa, T., Janka, H.-T., Müller, E. 2003, A&A, 408, 621
- Kitaura, F. S., Janka, H.-Th. & Hillebrandt, W., 2006, A&A, 450, 345
- Kiuchi, K. & Kotake, K. 2008, MNRAS, 385, 1327
- Kuroda, T., Kotake, K., & Takiwaki, T. 2012, arXiv:1202.2487, accepted by ApJ
- Kotake, K., Yamada, S., & Sato, K. 2003, ApJ, 595, 304
- Kotake, K., Yamada, S., Sato, K., et al. 2004, Phys. Rev. D, 69, 124004
- Kotake, K., Sawai, H., Yamada, S., & Sato, K. 2004, Astrophys. J., 608, 391
- Kotake, K., Sato, K., & Takahashi, K. 2006, Reports of Progress in Physics, 69, 971
- Kotake, K., Iwakami, W., Ohnishi, N., & Yamada, S. 2009, ApJ, 697, L133
- Kotake, K., Iwakami, W., Ohnishi, N., & Yamada, S. 2009, ApJ, 704, 951
- Kotake, K. 2011, arXiv:1110.5107, accepted by Comptes Rendus Physique
- Kotake, K., Iwakami-Nakano, W., & Ohnishi, N. 2011, ApJ, 736, 124
- Kotake, K., Takiwaki, T., Suwa, Y., et al. 2012, arXiv:1204.2330, accepted by Advances in Astronomy
- Kotake, K., Sumiyoshi, K., Yamada, S., et al. 2012, arXiv:1205.6284, accepted by Progress in Theoretical and Experimental Physics
- Kotake, K., Takiwaki, T., & Harikae, S. 2012, arXiv:1205.6061, accepted by ApJ
- Langanke, K., Martínez-Pinedo, G., Müller, B., et al. 2008, Physical Review Letters, 100, 011101
- Lattimer, J. M. & Swesty, F. D. 1991, Nuclear Physics A, 535, 331
- Lattimer, J. M., & Lim, Y. 2012, arXiv:1203.4286
- Lentz, E. J., Mezzacappa, A., Bronson Messer, O. E., et al. 2011, arXiv:1112.3595

- Levermore, C. D., 1984, *Journal of Quantitative Spectroscopy and Radiative Transfer*, 31, 149
- Liebendörfer, M., Mezzacappa, A., Thielemann, F.-K., Messer, O. E., Hix, W. R. & Bruenn, S. W., 2000, *Phys. Rev. D*, 63, 103004
- Liebendörfer, M., Mezzacappa, A., Thielemann, F.-K., et al. 2001, *Phys. Rev. D*, 63, 103004
- Liebendörfer, M., Messer, O. E. B., Mezzacappa, A., et al. 2004, *ApJS*, 150, 263
- Liebendörfer, M., Rampp, M., Janka, H.-Th., & Mezzacappa, A., 2005, *ApJ*, 620, 840
- Liebendörfer, M. 2005, *ApJ*, 633, 1042
- Liebendörfer, M., Whitehouse, S. C., & Fischer, T. 2009, *ApJ*, 698, 1174
- Limongi, M. & Chieffi, A. 2006, *Astrophys. J.*, 647, 483
- Lund, T., Marek, A., Lunardini, C., Janka, H.-T., & Raffelt, G. 2010, *Phys. Rev. D*, 82, 063007
- Marek, A. & Janka, H.-Th., 2009, *ApJ*, 694, 664
- Marek, A., Janka, H.-T., Müller, E. 2009, *A&A*, 496, 475
- Mezzacappa, A., Bruenn, S. W., Blondin, J. M., Hix, W. R., & Bronson Messer, O. E. 2007, in *American Institute of Physics Conference Series*, Vol. 924, *The Multicolored Landscape of Compact Objects and Their Explosive Origins*, ed. T. di Salvo, G. L. Israel, L. Piersant, L. Burderi, G. Matt, A. Tornambe, & M. T. Menna, 234–242
- Mueller, B., Janka, H.-T., Marek, A., et al. 2011, *arXiv:1112.1913*
- Mueller, B., Janka, H.-T., & Heger, A. 2012, *arXiv:1205.7078*
- Mueller, B., Janka, H.-T., & Heger, A. 2012, *arXiv:1205.7078*
- Müller, E., Janka, H.-T., & Wongwathanarat, A. 2012, *A&A*, 537, A63
- Murphy, J. W., & Burrows, A., 2008, *ApJ*, 688, 1159
- Nakamura, S. X., Sumiyoshi, K., & Sato, T. 2009, *Phys. Rev. C*, 80, 035802
- Nomoto, K. & Mashimoto, M. 1988, *Phys. Rep.*, 163, 13
- Nordhaus, J., Burrows, A., Almgren, A. & Bell, J., 2010, *ApJ*, 720, 694

- Obergaulinger, M. & Janka, H.-T. 2011, ArXiv e-prints
- O’Connor, E. & Ott, C. D. 2011, ApJ, 730, 70
- Ohnishi, N., Kotake, K. & Yamada, S., 2006, ApJ, 641, 1018
- . 2007, ApJ, 667, 375
- Ott, C. D., Abdikamalov, E., O’Connor, E., et al. 2012, arXiv:1204.0512
- Sato, J., Foglizzo, T., & Fromang, S. 2009, ApJ, 694, 833
- Scheck, L., Plewa, T., Janka, H.-T., Kifonidis, K., & Müller, E., 2004, Phys. Rev. Lett., 92, 011103
- Scheck, L., Kifonidis, K., Janka, H., & Müller, E. 2006, A&A, 457, 963
- Scheck, L., Janka, H.-T., Foglizzo, T. & Kifonidis, K., 2008, A&A, 477, 931
- Shen, H., Toki, H., Oyamatsu, K. & Sumiyoshi, K., 1998, Nucl. Phys. A, 637, 435
- Steiner, A. W., Lattimer, J. M., & Brown, E. F. 2010, ApJ, 722, 33
- Sumiyoshi, K., & Yamada, S. 2012, ApJS, 199, 17
- Sagert, I., Fischer, T., Hempel, M., Pagliara, G., Schaffner-Bielich, J., Mezzacappa, A., Thielemann, F., & Liebendörfer, M. 2009, Physical Review Letters, 102, 081101
- Sumiyoshi, K. & Röpke, G. 2008, Phys. Rev. C, 77, 055804
- Sumiyoshi, K., Yamada, S., Suzuki, H., Shen, H., Chiba, S. & Toki, H., 2005, ApJ, 629, 922
- Suzuki, T. K., Sumiyoshi, K., & Yamada, S. 2008, ApJ, 678, 1200
- Suwa, Y., Kotake, K., Takiwaki, T., Whitehouse, S. C., Liebendörfer, M. & Sato, K., 2010, PASJ, 62, L49
- Suwa, Y., Kotake, K., Takiwaki, T., Liebendörfer, M., & Sato, K. 2011, ApJ, 738, 165
- Suwa, Y., Takiwaki, T., Kotake, K., et al. 2012, arXiv:1206.6101
- Tanaka, M., Kawabata, K. S., Hattori, T., et al. 2012, arXiv:1205.4111
- Takahara, M. & Sato, K. 1988, Progress of Theoretical Physics, 80, 861
- Takiwaki, T., Kotake, K., Nagataki, S., & Sato, K. 2004, ApJ, 616, 1086

- Takiwaki, T., Kotake, K., & Sato, K. 2009, *Astrophys. J.*, 691, 1360
- Takiwaki, T., Kotake, K., & Suwa, Y. 2012, *ApJ*, 749, 98
- Takiwaki, T., & Kotake, K. 2011, *ApJ*, 743, 30
- Thompson, T. A., Burrows, A., & Pinto, P. A. 2003, *Astrophys. J.*, 592, 434
- Thompson, T. A., Quataert, E., & Burrows, A. 2005, *ApJ*, 620, 861
- Rampp, M. & Janka, H.-Th., 2000, *ApJ*, 539, L33
- Rauscher, T. & Thielemann, F.-K. 2000, *Atomic Data and Nuclear Data Tables*, 75, 1
- Wang, L. & Wheeler, J. C. 2008, *ARA&A*, 46, 433
- Wilson, J. R. 1985, in *Numerical Astrophysics*, 422–+
- Wongwathanarat, A., Janka, H.-T., Müller, E. 2010, *ApJ*, 725, L106
- Woosley, S. E. & Weaver, T. A., 1995, *ApJS*, 101, 181
- Woosley, S. E., Heger, A., & Weaver, T. A. 2002, *Reviews of Modern Physics*, 74, 1015